Journal of Materials Chemistry B

ROYAL SOCIETY OF CHEMISTRY

PAPER

View Article Online
View Journal | View Issue

Cite this: J. Mater. Chem. B, 2025, 13, 15397

Development and *in vitro*/*in vivo* evaluation of a triply periodic minimal surface-based 3D-printed anti-infective bone scaffold with spatiotemporally controlled osteogenesis

Peijie Zhao,[abcd] Mei Tian,[ac] Huan He,[ac] Jing Zhang,[ac] Bin Zhao,[ac] Huanhuan Sun,[ab] Zhipeng Yang[ab] and Zewen Qiao *[b]

Received 15th September 2025,
Accepted 28th October 2025

DOI: 10.1039/d5tb02071a

rsc.li/materials-b

Infectious bone defects (IBDs), marked by the concurrent presence and progressive aggravation of both bone infection and bone loss, represent a significant clinical challenge. Traditional staged treatment, namely initial infection control followed by bone reconstruction, often involves multiple surgeries, extended treatment durations, and high costs. Herein, we developed a novel 3D-printed titanium alloy scaffold for IBDs, integrating spatiotemporally controlled dual-drug delivery. The scaffold features a triply periodic minimal surface structure with a radial pore gradient, increasing from the core to the periphery. The inner layer with smaller pores is loaded with bone morphogenetic protein-2 (BMP-2), whereas the outer layer with larger pores incorporates RM-PLGA microspheres for the sustained release of rifampicin and moxifloxacin. The gelatin methacryloyl (GelMA) hydrogel serves as the coating matrix for drug immobilization. This design enables a sequential therapeutic strategy, initial sustained antibacterial activity, followed by osteoinductive stimulation, facilitating a dynamic repair process from early infection control to later-stage bone regeneration. *In vitro* assays confirmed that the RM-PLGA/BMP-2 (GelMA)@TiS scaffold exhibits potent antibacterial activity, cytocompatibility, osteogenic potential, and extracellular matrix mineralization. *In vivo* results further demonstrated its efficacy in suppressing *Staphylococcus aureus* infection while promoting bone regeneration.

1. Introduction

Infectious bone defects (IBDs) represent a complex clinical condition frequently encountered in orthopedic practice.[1] IBDs primarily arise from two causes: (1) severe open fractures resulting from high-energy trauma that are inadequately managed and (2) the increasing incidence of orthopedic implant surgeries, which may lead to chronic osteomyelitis and, eventually, IBDs.[2,3] The pathological progression of IBDs severely disrupts the local microenvironment, leading to an imbalance between osteoblastic and osteoclastic activities and thereby impairing bone formation while promoting bone resorption. This cascade results in progressive infection and bone degradation. The concurrent presence of infection and bone defects considerably complicates treatment, while the prolonged disease course and poor prognosis place considerable burdens on both patients and clinicians.[4] The standard treatment strategy for IBDs involves infection control followed by reconstruction of the bone defect. Common approaches include the Masquelet technique and bone transport.[5] However, both methods have several limitations: incomplete infection clearance, poor graft integration, limited availability of autologous bone, donor site morbidity, extended treatment duration, and difficulties in regenerating bone at the transport site. These challenges often lead to prolonged recovery, increased healthcare costs, psychological distress, and suboptimal outcomes. The Masquelet technique incorporates local antibiotic delivery through sustained-release carriers, offering a promising method for managing bone infections. Nevertheless, the use of polymethylmethacrylate bone cement as the antibiotic carrier has notable disadvantages, such as inconsistent drug release kinetics, limited compatibility with various antibiotics, and non-biodegradability.[6,7] These issues can result in incomplete eradication of infection, development of antibiotic-resistant bacteria, and persistence or formation of bacterial biofilms.

The advent of 3D bioprinting has provided innovative solutions for the clinical management of bone defects, enabling the fabrication of functionalized bone scaffolds tailored to specific pathological conditions, such as bone tumors, osteochondral

[a] Ningxia Medical University, Yinchuan, Ningxia, China
[b] Department of Hand Foot Ankle Surgical Ward, General Hospital of Ningxia Medical University, Yinchuan, Ningxia, China. E-mail: 13995307859@163.com
[c] Ningxia Key Laboratory of Clinical and Pathogenic Microbiology, Institute of Medical Sciences, General Hospital of Ningxia Medical University, Yinchuan, Ningxia, China
[d] Institute of Clinical Pharmacology, Department of Pharmacy, General Hospital of Ningxia Medical University, Yinchuan, Ningxia, China

defects, and osteomyelitis.[8,9] In the context of IBDs, scaffolds incorporating antibiotics and multiple growth factors have shown particularly promising therapeutic potential. Antibiotic-loaded scaffolds offer the advantage of localized, high-concentration drug delivery, thereby significantly enhancing antimicrobial efficacy.[10] Additionally, the controlled release of osteoinductive factors supports and accelerates bone regeneration.[11,12]

From a pathological perspective, infection inherently impairs bone healing, making high local concentrations of antibiotics essential during the early stages of IBD treatment.[13] However, conventional anti-infective scaffolds often exhibit uncontrolled or poorly synchronized release of antibiotics and osteogenic factors, thereby limiting their therapeutic efficacy. This underscores the urgent need for advanced multi-layered, multi-gradient controlled-release systems (enabled by 3D bioprinting) to deliver bioactive agents in a temporally and spatially coordinated manner. Such systems can provide phase-specific therapeutic effects, ensuring precise infection control during the early stage and promoting targeted bone regeneration thereafter.[14] Implementing this dual-phase therapeutic strategy in a single surgical intervention holds significant clinical promise by accelerating both infection resolution and bone healing, shortening treatment duration, reducing healthcare costs, and improving patient outcomes.[15]

To develop a dynamic bone scaffold capable of temporal functional switching from an early-stage antibacterial action to mid-to-late-stage osteogenesis, a novel design strategy was employed in this study. Two broad-spectrum antibiotics with high intraosseous bioavailability, moxifloxacin (Mox) and rifampicin (Rif), were encapsulated in poly(lactic-*co*-glycolic) acid (PLGA) to form RM-PLGA microspheres *via* a controlled fabrication process. A triply periodic minimal surface (TPMS) structure with a radially increasing porosity gradient was fabricated using 3D bioprinting. The resulting scaffold measured 15 mm in diameter, 2 mm in height, and featured porosity ranging from 55% at the core to 90% at the periphery. The gelatin methacryloyl (GelMA) hydrogel served as a carrier for incorporating both RM-PLGA microspheres and bone morphogenetic protein-2 (BMP-2) into the scaffold. RM-PLGA microspheres were embedded in the outer layer to enable early-stage sustained antibiotic release, establishing a favorable microenvironment for subsequent osteogenesis. BMP-2 was loaded into the inner layer to promote osteoinduction during the mid-to-late stages, with residual RM-PLGA microspheres providing continued antibacterial protection. Comprehensive *in vitro* evaluations assessed scaffold morphology, loading capacity (LC), release kinetics, cytocompatibility, osteoinductive potential, and antibacterial efficacy. To verify *in vivo* performance, an infectious cranial bone defect model was established in New Zealand white rabbits. General physiological parameters, microbiological assays, histological analyses, and radiological imaging were performed to comprehensively evaluate the scaffold's anti-infective and bone-regenerative capabilities.

2. Materials and methods

2.1. Materials

PLGA was obtained from Daigang Biomaterial (Jinan, China). BMP-2 was purchased from MedChemExpress (New Jersey, America), and Mox and Rif were acquired from Aladdin Scientific (Shanghai, China) and Yuanye Biological Technology (Shanghai, China), respectively. GelMA was supplied by EFL (Suzhou, China). The MC3T3-E1 subclone 14 pre-osteoblast cell line (RRID: CVCL-0022) was obtained from iCell Bioscience (Shanghai, China).

2.2. Experimental methods

2.2.1. Preparation and characterization of RM-PLGA microspheres. RM-PLGA microspheres were prepared using a double emulsion solvent evaporation method, as detailed in Appendix S1.[16] Briefly, 10 mg of dried microspheres were dispersed in 5 mL of phosphate-buffered saline (PBS), followed by ultrasonic disruption for 2 hours and incubation at room temperature for 24 hours. The suspension was then centrifuged for 10 minutes, and the supernatant was collected and diluted 20-fold. The concentrations of Mox and Rif were measured using ultraviolet-visible (UV-Vis) spectrophotometry. The drug loading (DL) and encapsulation efficiency (EE) were calculated as follows: DL = (mass of Mox in microspheres/total mass of drug-loaded PLGA microspheres) × 100%; EE = (mass of Mox in microspheres/total mass of Mox initially added) × 100%.[17] For morphological analysis, dried microspheres were mounted on a conductive adhesive film, sputter-coated with gold under vacuum, and examined *via* scanning electron microscopy (SEM, S-3400N, Hitachi Co., Japan) at an accelerating voltage of 10.0 kV. Particle size distribution was also analyzed.[18]

2.2.2. Preparation of GelMA hydrogel solutions and determination of the optimal concentration. GelMA hydrogel solutions at concentrations of 5%, 10%, and 15% (w/v) were prepared by dissolving 5, 10, and 15 g of GelMA, respectively, in light-protected centrifuge tubes containing 0.05 g of photoinitiator. The mixtures were heated in a 65 °C water bath for 30 minutes until fully dissolved. Each hydrogel formulation was then co-cultured with MC3T3-E1 cells (non-pollution) for 24 hours, followed by assessment of cell viability using a CCK-8 proliferation assay (Fig. S1). Optical density (OD) was measured at 450 nm using a microplate reader. Among the tested concentrations, the 10% (w/v) GelMA hydrogel showed the highest cell viability and was thus selected for all subsequent experiments.[19]

2.2.3. Optimization of the BMP-2 concentration. A total of 10 μg of BMP-2 lyophilized powder was dissolved in 20 μL of the supplied solvent and subsequently diluted with 80 μL of PBS containing 5% carrier protein to prepare a 100 μg mL^{-1} BMP-2 stock solution. Working solutions of 50, 100, 150, and 200 ng mL^{-1} were then prepared by adding 0.5, 1.0, 1.5, and 2.0 μL of the stock solution to 1000 μL of PBS, respectively. MC3T3-E1 cells were co-cultured with each concentration for 24 hours, followed by assessment of cell viability using a CCK-8 proliferation assay (Fig. S2). The OD values at 450 nm were measured using a microplate reader. The 150 ng mL^{-1} BMP-2 group exhibited the highest OD value, indicating optimal cell proliferation, and was therefore selected for all subsequent experiments.[20,21]

2.2.4. Fabrication and grouping of composite scaffolds. TPMS scaffolds were fabricated using selective laser melting (SLM) with Ti–6Al–4V powder as the building material.[22] The sample was constructed layer by layer with a 30 μm laser spot. Specifically, the printing laser power was 100 W, the hatch spacing was 70 μm, the laser scanning speed was 400 mm s^{-1}, the board temperature was 35 °C, and the alternate hatch mode was adopted as the scanning strategy. Following high-pressure steam sterilization and drying, the titanium scaffolds were placed in flat-bottom containers. A 1 mL GelMA hydrogel solution containing 20 μL of 150 ng mL^{-1} BMP-2 was added to each container, and gentle agitation was applied using a shaker to ensure uniform coating and infiltration of the scaffold. The hydrogel was then photo-crosslinked using a 405 nm UV flashlight, resulting in a partially modified scaffold. After 24 hours, an additional 1 mL of GelMA hydrogel containing 20 mg of RM-PLGA microspheres was added and similarly photo-crosslinked under 405 nm UV light to yield the final RM-PLGA/BMP-2(GelMA)@TiS scaffold.[23] The experimental groups were as follows: RM-PLGA/BMP-2(GelMA)@TiS, BMP-2(GelMA)@TiS, RM-PLGA(GelMA)@TiS, and TiS (unmodified scaffold).

2.3. Evaluation of drug release performance

2.3.1. Antibiotic release profile. Scaffolds were placed in dialysis bags containing 1 mL of PBS, sealed, and immersed in polyethylene tubes filled with 5 mL of PBS. The tubes were incubated under gentle shaking. At predetermined time points, the external PBS solution was collected and analyzed using UV-Vis spectrophotometry to quantify the concentrations of Mox and Rif released (Appendix S2). The cumulative drug release was calculated as follows: release = $(m_1/m_2) \times 100\%$, where m_1 is the amount of drugs released into the external PBS, and m_2 is the total amount of drug initially loaded into the microspheres.[24,25]

2.3.2. BMP-2 release profile. Composite scaffolds were incubated in 1 mL of deionized water. At predetermined time points (days 1, 3, 5, 7, 14, 21, and 28), the supernatant was collected and replaced with an equal volume of fresh buffer. The concentration of BMP-2 in the collected supernatant was quantified using a BMP-2 ELISA kit[26] (Appendix S3).

2.4. Morphological and structural characterization of the composite scaffold

Dried RM-PLGA/BMP-2(GelMA)@TiS scaffolds were mounted onto conductive adhesive films and sputter-coated with gold under vacuum. Scaffold morphology was examined using SEM, and elemental composition was analyzed using energy-dispersive spectroscopy (EDS).[27]

2.5. *In vitro* evaluation of biological performance

MC3T3-E1 subclone 14 cells were rapidly thawed and cultured in a cell incubator under standard conditions. Sterilized scaffolds from each experimental group were placed in 12-well plates, and 100 μL of the cell suspension (1×10^5 cells per mL) was seeded onto the surface of each scaffold. After 24 hours of co-culture, the scaffolds were fixed in glutaraldehyde for 24 hours, followed by dehydration, gold sputter-coating, and SEM to evaluate cell adhesion on the scaffold surfaces. Cell viability on days 1 and 3 was assessed using live/dead staining and visualized with a fluorescence microscope. Cytotoxicity and cell proliferation were evaluated using CCK-8 assays on days 1, 3, 5, and 7, with OD measured at 450 nm using a microplate reader. Additionally, after 24 hours of co-culture, cells on the scaffolds were fixed with 4% paraformaldehyde (PFA) for 10 minutes and stained with Actin-Tracker Red and DAPI (4′,6-diamidino-2-phenylindole) to visualize the cytoskeleton and nuclei, respectively. Stained cells were then observed under a fluorescence microscope.

2.6. Effects of scaffolds on osteogenic differentiation

Scaffolds were placed in the upper chambers of transwell inserts, and 100 μL of the MC3T3-E1 cell suspension (1×10^5 cells per mL) was seeded into the lower chambers. After 24 hours of incubation, the culture medium was replaced with osteogenic induction medium, which was refreshed every 3 days. To assess osteogenic differentiation, sirius red staining was performed on day 7 to evaluate collagen deposition. Samples were imaged under a microscope, washed with 0.1 M acetic acid, and the bound dye was eluted using a 0.2 M sodium hydroxide/methanol solution. The OD was measured at 540 nm. On days 7 and 12, alkaline phosphatase (ALP) activity was assessed using an ALP detection kit, with stained samples imaged microscopically and OD values measured at 405 nm. On days 21 and 28, alizarin red S staining was performed to detect calcium deposition, followed by imaging and dye elution using cetylpyridinium chloride. The OD was then measured at 620 nm to quantify mineralization.

2.7. *In vitro* antibacterial evaluation

Staphylococcus aureus (SA) stock solution was rapidly thawed and cultured on tryptic soy agar (TSA) plates. After incubation at 37 °C for 24 hours, pure SA colonies were obtained and gently collected using sterile cotton swabs and then suspended in sterile PBS. The bacterial suspension was transferred to a turbidity tube for OD adjustment. Sterilized scaffolds from each experimental group were placed in 6-well plates, and 3 mL of the SA suspension (1.0×10^8 CFU mL^{-1}) was added to each well. After 24 hours of co-culture, the bacterial suspensions were serially diluted 10-fold and 100-fold; 100 μL of each dilution was spread onto TSA plates and incubated for 24 hours, after which colony-forming units (CFUs) were counted to calculate the antibacterial rate. For inhibition zone analysis, 100 L of the bacterial suspension (1.0×10^8 CFU mL^{-1}) was evenly spread onto TSA plates, and each scaffold was placed at the center of a plate; the blank control group received no scaffold. After 24 hours of incubation, the diameter of the inhibition zones surrounding each scaffold was measured. For biofilm formation analysis, 1 mL of the bacterial suspension and a scaffold were added to each well of a 24-well plate and incubated for 24 hours. Scaffolds were then fixed with 4% PFA for 20 minutes, stained with 0.5% crystal violet at room temperature for 10 minutes, and observed under a microscope. The biofilms were subsequently solubilized using 33% acetic acid,

and the OD was measured at 575 nm using a microplate reader. To directly observe biofilm morphology, scaffolds co-cultured with bacteria for 24 hours were fixed in glutaraldehyde for 24 hours, dehydrated, sputter-coated with gold, and examined *via* SEM. To assess bacterial viability, scaffolds were co-cultured with 1 mL of the SA suspension in 24-well plates for 24 hours, stained with a SYTO 9/PI bacterial viability kit, and observed under a fluorescence microscope to distinguish live from dead bacteria.

2.8. Establishment of the infectious cranial bone defect model

All animal experiments were approved by the Institutional Animal Care and Use Committee (Approval no. IACUC-NYLAC-2024-215).[28] The duration of the animal experiments is from November 8, 2024 to May 9, 2025.The anesthesia method was inhalation of anesthesia with 10% isoflurane. An infectious cranial bone defect model was established in male New Zealand white rabbits (Fig. S3). All animals were procured from the Experimental Animal Center of Ningxia Medical University. Animal housing and experimental procedures were conducted in accordance with national guidelines for the care and use of laboratory animals issued by relevant research authorities.

After anesthesia, 8-week-old New Zealand white rabbits were subjected to a midline scalp incision and periosteal reflection to fully expose the frontal and parietal bones. Using a cranial trephine, a full-thickness circular bone defect with a diameter of 15 mm was created in the calvarium. Composite scaffolds from the four experimental groups were implanted into the defect area, and 100 μL of the SA suspension (1×10^8 CFU mL^{-1}) was inoculated onto each scaffold to induce local infection. Two weeks postoperatively, skin and subcutaneous tissue surrounding the surgical site were harvested for histological analysis. Hematoxylin–eosin (H&E) and Giemsa staining were performed to assess local inflammation. Additionally, the soft tissues were rolled onto blood agar plates and incubated for 24 hours to observe and quantify bacterial colony formation. At postoperative weeks 7 and 14, the animals were euthanized, and tissue specimens centered on the defect site were harvested, trimmed to approximately 50 mm × 30 mm, and fixed in 4% PFA. Specimens were subjected to X-ray imaging and micro-computed tomography (micro-CT) scanning. Three-dimensional reconstruction of the defect area was performed using MIMICS software, with newly formed bone digitally segmented and labeled in red. Bone microarchitecture was quantitatively analyzed using CTAn software to calculate the trabecular thickness (Tb.Th), trabecular number (Tb.N), and bone volume (BV) as a percentage of total volume (TV) within the region of interest. For molecular analysis, bone tissue from the scaffold periphery and internal pores was carefully harvested and ground into fine powder using a mortar pre-cooled with liquid nitrogen. Total protein was extracted using lysis buffer, and osteogenic markers, including Runx2, osteocalcin (OST), and osteopontin (OPN), were analyzed *via* western blotting (WB) and quantitative polymerase chain reaction (qPCR) (Table S1). Cranial bone specimens were also fixed in 4% PFA for 24 hours, followed by standard dehydration procedures. Histological evaluations included H&E staining, Masson's trichrome staining, and van Gieson (VG) staining. Stained sections were imaged under a light microscope, and ImageJ software was used to quantify the area of newly formed bone within each scaffold. The percentage of new bone tissue was calculated relative to the total field of view.

2.9. Statistical analysis

All data are expressed as mean ± standard deviation ($\bar{x} \pm s$). One-way analysis of variance, followed by Tukey's post hoc test, was used to determine statistical significance between groups. A *P*-value of less than 0.05 was considered statistically significant. Significance levels are indicated as follows: $^{*}P < 0.05$, $^{**}P < 0.01$, $^{***}P < 0.001$, $^{****}P < 0.0001$; "ns" denotes no significant difference.

3. Results

3.1. Fabrication and characterization of RM-PLGA/BMP-2(GelMA)@TiS scaffolds

In this study, RM-PLGA microspheres were prepared using a double emulsion solvent evaporation method (Fig. 1G). PLGA (Fig. 1A) was used as a carrier to encapsulate two broad-spectrum antibiotics—Mox (Fig. 1C) and Rif (Fig. 1B), both known for their high intraosseous bioavailability. PLGA is a transparent, odorless crystalline polymer that was dissolved in an inner-phase solution of acetonitrile and isopropanol (Fig. 1E). Both Mox, a fine white powder, and Rif, a dark red powder, were incorporated into the inner-phase solution (Fig. 1F). The outer-phase solution was formulated using petroleum ether (30–60 °C), liquid paraffin, and Span 85 (Fig. 1D). Gelatin appears as a colorless, odorless, lightweight, and porous white solid (Fig. 1H). SEM revealed that the RM-PLGA microspheres were spherical with moderately smooth surfaces (Fig. 2A). The average diameter of the microspheres was 21.47 μm (Fig. 2B). The LC of Mox within the RM-PLGA microspheres was 4.08% ± 0.52%, while that of Rif was 5.09% ± 0.61%, with corresponding encapsulation efficiencies of 41.07% ± 4.72% and 51.40% ± 9.64%, respectively. A TPMS scaffold with a G-type unit cell was fabricated using SLM (Fig. 1I). The scaffold featured a porosity gradient increasing radially from the center (ranging from 55% to 90%) and an internal pore size distribution of 420–630 μm. The final scaffold had a mechanically rigid texture, with dimensions of 15 × 2 mm. SEM images (Fig. 2D) confirmed that the RM-PLGA microspheres were predominantly localized to the outer layer of the scaffold, whereas BMP-2 was uniformly distributed within the inner layer. Moreover, the GelMA hydrogel effectively filled the scaffold's porous architecture. EDS (Fig. 2H) detected the presence of titanium (Ti), carbon (C), oxygen (O), nitrogen (N), chlorine (Cl), potassium (K), sodium (Na), and phosphorus (P) on the surface of the RM-PLGA/BMP-2(GelMA)@TiS scaffold, further confirming the successful loading of both RM-PLGA and BMP-2 *via* the hydrogel onto the titanium scaffold. The macroscopic appearances of the four scaffold types—RM-PLGA/BMP-2(GelMA)@TiS, BMP-2(GelMA)@TiS, RM-PLGA(GelMA)@TiS, and unmodified TiS—are

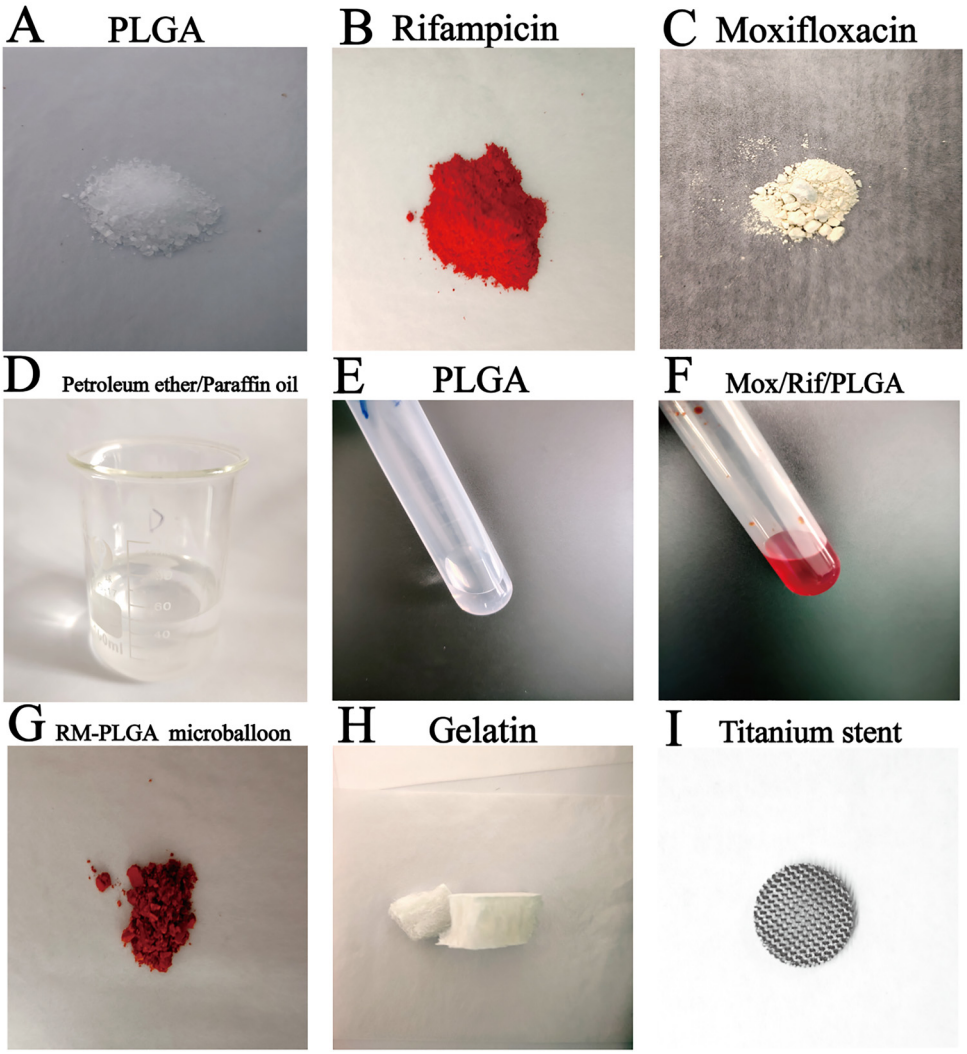

Fig. 1 (A) A view of the PLGA solid. (B) A view of the rifampicin solid. (C) A view of the moxifloxacin solid. (D) A view of moxifloxacin dissolved in petroleum ether and liquid paraffin. (E) A view of PLGA dissolved in acetonitrile and isopropanol. (F) A view of moxifloxacin and rifampicin added to PLGA solution. (G) A view of moxifloxacin/rifampicin microspheres. (H) A view of the gelatin solid. (I) A view of the titanium scaffold solid.

shown in (Fig. 2C). The BMP-2 release profiles (Fig. 3E) revealed distinct temporal differences between the two BMP-2-loaded groups. In the BMP-2(GelMA)@TiS group, no significant BMP-2 release was observed within the first 30 hours; the release began around 48 hours and continued in a rapid and sustained manner until day 18, after which the release rate gradually declined. In contrast, the RM-PLGA/BMP-2(GelMA)@TiS group exhibited a delayed onset of release, with minimal BMP-2 released during the first 8 days; the rapid release began on day 9 and continued thereafter. Notably, the RM-PLGA/BMP-2(GelMA)@TiS group consistently retained higher levels of BMP-2 at equivalent time points. This might be explained by the spatial configuration of RM-PLGA/BMP-2(GelMA)@TiS. BMP-2 is embedded in the inner layer, while RM-PLGA microspheres are embedded in the outer layer. This configuration effectively delays BMP-2 diffusion and minimizes early-stage burst release. The release profiles of Mox and Rif are shown in Fig. 2F and Fig. 2G, respectively. Both RM-PLGA/BMP-2(GelMA)@TiS and RM-PLGA(GelMA)@TiS exhibited early onset of drug release, but not in the form of a rapid burst. Instead, both antibiotics followed a pattern of sustained release, extending gradually over a 28-day period. By day 21, the RM-PLGA(GelMA)@TiS group had released approximately 89% of Mox and 87.3% of Rif. In contrast, the RM-PLGA/BMP-2(GelMA)@TiS group reached similar cumulative release levels only by day 28. This delay is likely attributed to the secondary release of BMP-2 in the mid-to-late stages, which may have indirectly influenced the sustained release behavior of the RM-PLGA microspheres. Further research is warranted to clarify whether this delay affects the antibacterial efficacy in subsequent antibacterial experiments.

3.2. *In vitro* biocompatibility of RM-PLGA/BMP-2(GelMA)@TiS scaffolds

The *in vitro* biocompatibility of the composite scaffolds was assessed using cellular adhesion, viability, cytotoxicity, and proliferation assays.

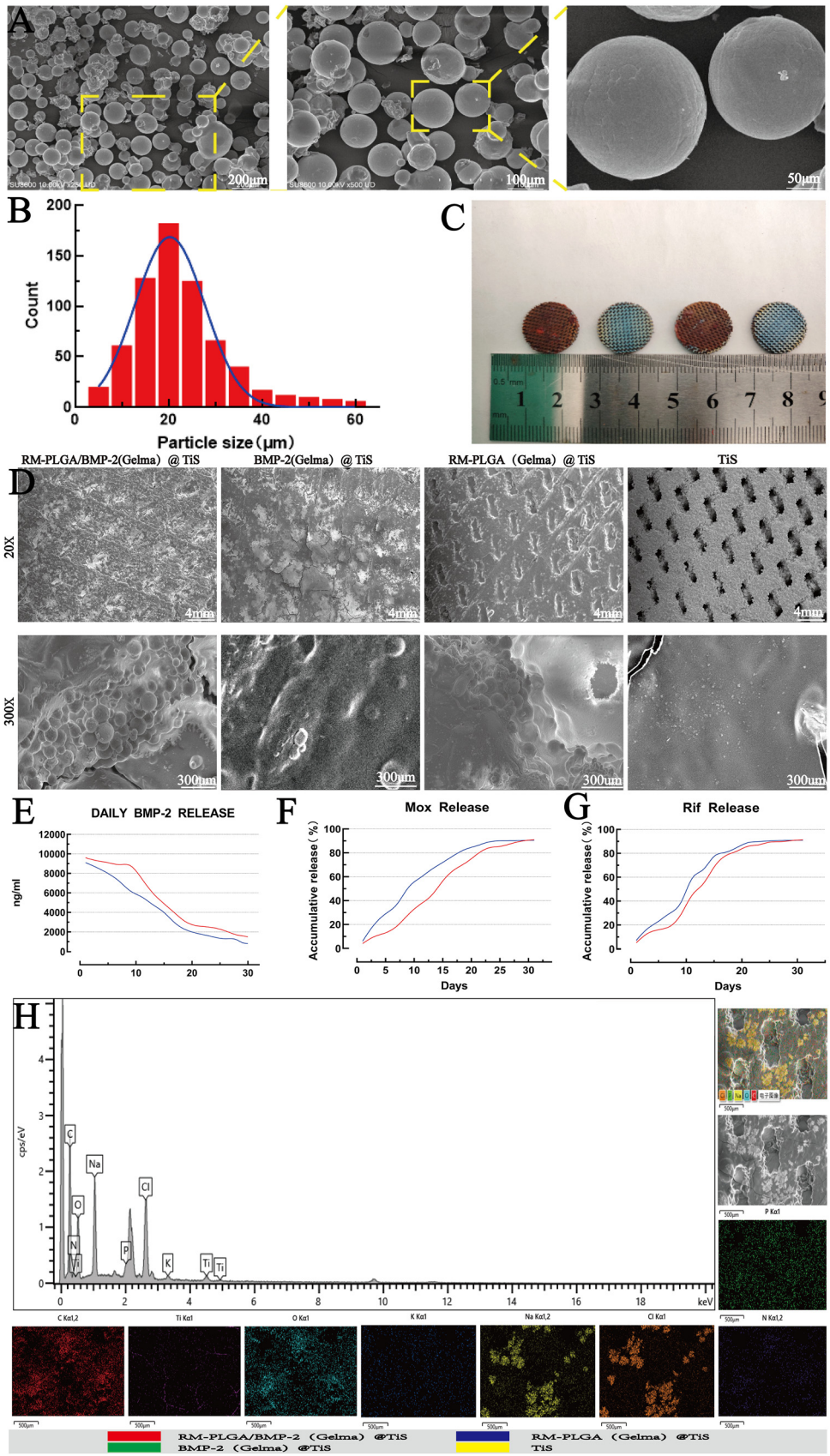

Fig. 2 (A) Scanning electron microscopy (SEM) image of RM-PLGA microspheres. (B) Particle size distribution of RM-PLGA microspheres. (C) Physical views of the four groups of scaffolds from left to right: RM-PLGA/BMP-2(Gelma)@TiS, BMP-2(Gelma)@TiS, RM-PLGA(Gelma)@TiS, and TiS group. (D) SEM images of the four groups of scaffolds. (E) BMP-2 release profiles of RM-PLGA/BMP-2(Gelma)@TiS and BMP-2(Gelma)@TiS. (F) Moxifloxacin release profiles of RM-PLGA/BMP-2(Gelma)@TiS and RM-PLGA(Gelma)@TiS. (G) Rifampicin release profiles of RM-PLGA/BMP-2(Gelma)@TiS and RM-PLGA(Gelma)@TiS. (H) Energy dispersive X-ray spectroscopy (EDS) scan of the RM-PLGA/BMP-2(Gelma)@TiS scaffold.

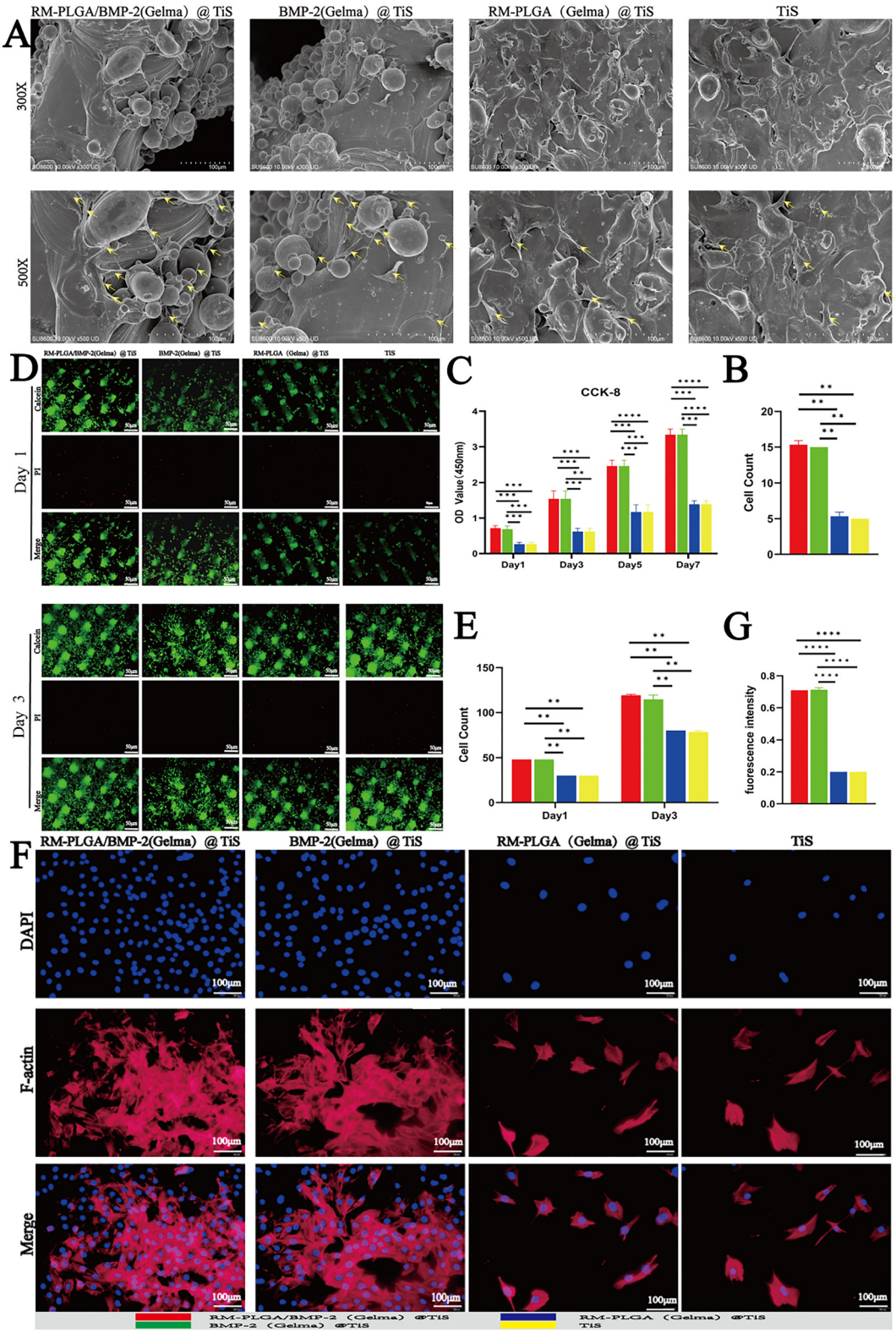

Fig. 3 (A) Scanning electron microscopy image of the composite scaffold co-cultured with cells. (B) Statistical graph of the number of cells adhered to the scaffold. (C) CCK-8 test results. (D) Live and dead cell staining images on the 1st and 3rd days. (E) Live and dead cell statistics on the 1st and 3rd days. (F) Cell morphology staining (blue represents the cell nucleus and red represents the cell skeleton). (G) Quantitative statistical analysis of cell fluorescence intensity, *$p < 0.05$, **$p < 0.01$, ***$p < 0.001$, $N = 3$.

SEM images (Fig. 3A) revealed that MC3T3-E1 cells adhered to the scaffold surface, exhibiting a short spindle-shaped morphology with prominent pseudopodia extensions. Slight surface cracking of the hydrogel was observed after drying. In all four groups (Fig. 3B), the cells demonstrated varying degrees of spreading and intercellular contact. Notably, the two BMP-2-loaded groups showed denser and more complex formation of cell membranes and interconnections, whereas

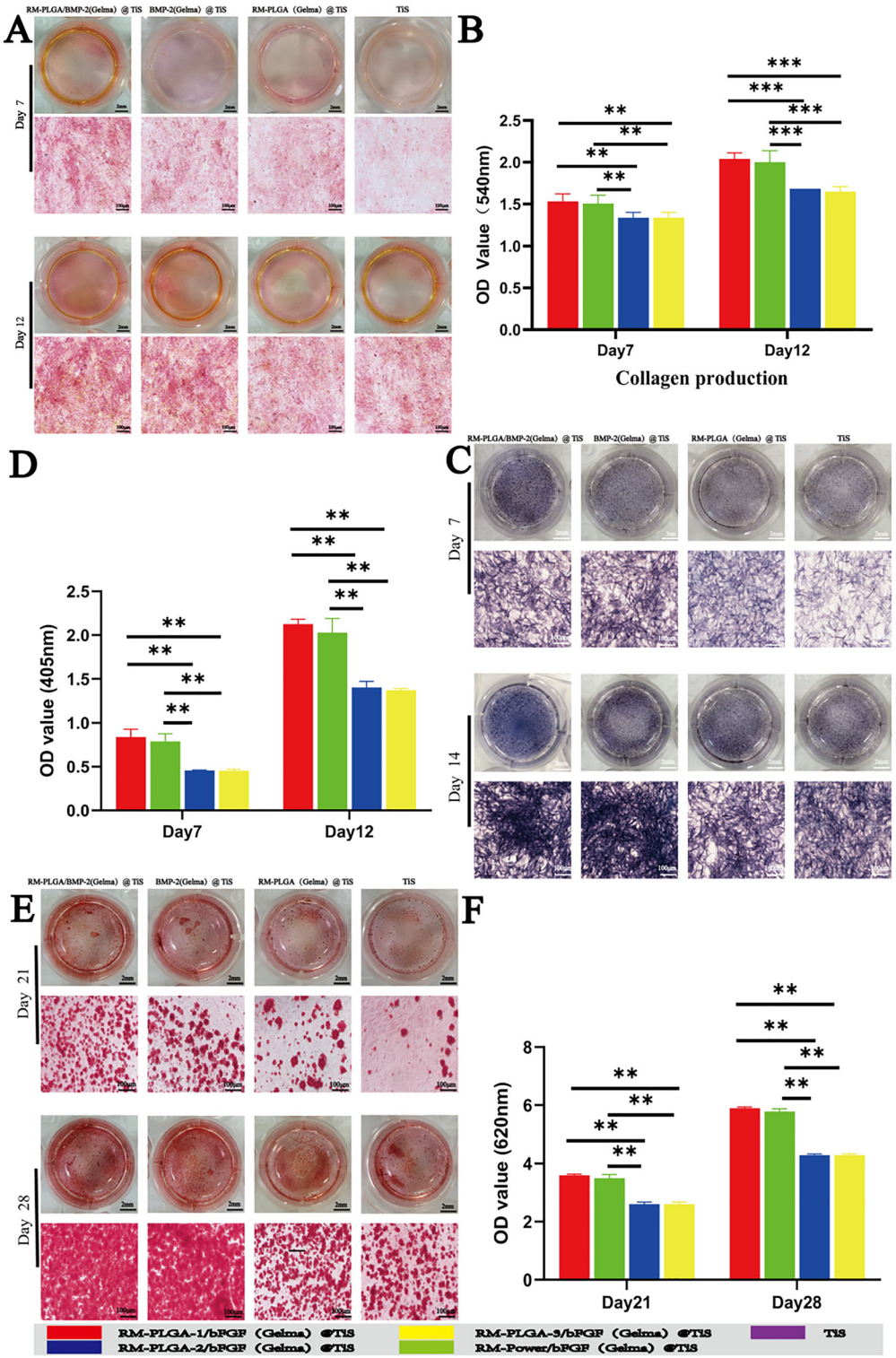

Fig. 4 (A) Result of sirius red staining. (B) Result of collagen secretion. (C) Result of ALP staining. (D) Quantitative detection result of ALP. (E) Result of alizarin red staining. (F) Quantitative detection result of calcium nodules. *$p < 0.05$, **$p < 0.01$, ***$p < 0.001$, $N = 3$.

the RM-PLGA(GelMA)@TiS group and the unmodified TiS group exhibited sparse cell attachment and minimal pseudopodia formation. Results of the CCK-8 assay (Fig. 3C) indicated that, on day 1, the RM-PLGA/BMP-2(GelMA)@TiS and BMP-2(GelMA)@TiS groups had significantly higher OD values compared with the other two groups. This trend persisted over time, with the BMP-2-loaded groups consistently outperforming the controls in terms of cell viability. Live/dead cell staining (Fig. 3D and E) showed that the RM-PLGA/BMP-2(GelMA)@TiS and BMP-2(GelMA)@TiS groups had abundant green-fluorescing cells (live cells) and extremely few red-stained dead cells on days 1 and 3. In contrast, the RM-PLGA(GelMA)@TiS and unmodified TiS groups exhibited considerably fewer live cells. Nuclear and cytoskeletal staining and fluorescence intensity analyses (Fig. 3F and G) further confirmed the enhanced biocompatibility observed in the RM-PLGA/BMP-2(GelMA)@TiS and BMP-2(GelMA)@TiS groups. Numerous blue-stained nuclei were surrounded by red-stained actin cytoskeletons, which appeared elongated and interwoven, with multiple pseudopodia protruding from the cell periphery. Compared with the other groups, cells in the BMP-2-loaded groups exhibited wider, longer cytoskeletal structures.

These results demonstrated that all four scaffold groups exhibited good biocompatibility. Notably, the RM-PLGA/BMP-2(GelMA)@TiS and BMP-2(GelMA)@TiS groups significantly enhanced cell proliferation.

3.3. Effects of RM-PLGA/BMP-2(GelMA)@TiS scaffolds on osteogenic differentiation of MC3T3-E1 cells

The osteogenic potential of the fabricated scaffolds was evaluated through collagen fiber staining, ALP staining, and analyses of calcium nodule formation.

Sirius red staining (Fig. 4A) on day 7 of osteogenic induction revealed pale pink-stained collagen fibers and faint yellow-stained myofibers in the RM-PLGA/BMP-2(GelMA)@TiS and BMP-2(GelMA)@TiS groups. In contrast, the unmodified TiS group showed only minimal, faint collagen fiber staining. By day 12, collagen deposition had increased substantially, manifesting as irregularly shaped, variably sized red-stained aggregates of collagen type I, especially in the RM-PLGA/BMP-2(GelMA)@TiS group. These findings were confirmed through quantitative analysis of sirius red dye elution. The OD values measured at 540 nm (Fig. 4B) in the RM-PLGA/BMP-2(GelMA)@TiS group were similar to those in the control groups.

The early osteogenic differentiation marker ALP was used to evaluate osteogenic activity after 7 and 12 days of induction.[29] On day 7, light blue ALP staining was clearly visible in the two BMP-2-loaded groups, which was a significant difference from the control groups. By day 12, MC3T3-E1 cells became more confluent and ALP staining appeared darker (Fig. 4C). The OD values of ALP-stained eluates at 405 nm further confirmed this trend (Fig. 4D).

Alizarin red S staining was performed after 21 days of osteogenic induction to determine the amount of calcium deposits, a late-stage osteogenic differentiation marker. Scattered red mineralized nodules were observed at the bottom of the culture wells, and intercellular membrane connections were seen in some regions.[30] Only a few mineralized nodules were present in the RM-PLGA(GelMA)@TiS and TiS groups. Conversely, by day 28, the RM-PLGA/BMP-2(GelMA)@TiS and BMP-2(GelMA)@TiS groups exhibited densely distributed, irregularly shaped mineralized nodules of varying sizes, many of which had merged into large interconnected clusters. In contrast, the control groups displayed significantly fewer mineralized nodules (Fig. 4E). The OD values of the eluted dye at 620 nm are shown in Fig. 4F.

Collectively, these results demonstrate that both the BMP-2-loaded scaffolds exhibited strong potential to induce osteogenic differentiation and mineralization.

3.4. *In vitro* antibacterial properties of RM-PLGA/BMP-2(GelMA)@TiS scaffolds

SEM imaging revealed that untreated SA appeared as well-defined spherical cells, often aggregated in clusters.[31] Conversely, SA inoculated on the RM-PLGA/BMP-2(GelMA)@TiS and RM-PLGA(GelMA)@TiS scaffolds exhibited signs of structural collapse and fragmentation. Residual bacterial debris appeared interwoven into a fibrous, mesh-like necrotic network across the field of view, with only a few intact bacterial cells remaining. In contrast, the BMP-2(GelMA)@TiS and unmodified TiS groups displayed abundant intact and spherical SA cells (Fig. 5A). The live bacteria are marked with red arrows and the dead bacteria are marked with yellow arrows. Biofilm staining using crystal violet (Fig. 5B) showed that the RM-PLGA/BMP-2(GelMA)@TiS and RM-PLGA(GelMA)@TiS scaffolds had dense accumulation of dark purple-stained biofilms, whereas the control groups only presented sparse biofilm formation. Semiquantitative analysis of biofilm biomass further confirmed the significant differences between these groups (Fig. 5C). Moreover, the bacteria from different groups showed variable growth when spread on TSA plates after 10-fold and 100-fold dilution (Fig. 5D). Only a few SA colonies were observed in the RM-PLGA-loaded groups, whereas extensive SA growth across the plates was recorded in the BMP-2(GelMA)@TiS and TiS groups. Statistical analysis (Fig. 5E and F) confirmed that the bacterial count in the RM-PLGA/BMP-2(GelMA)@TiS group was significantly lower than that in the control groups, indicating that the composite scaffold possessed potent antibacterial activity.

In the zone of inhibition assays, no visible antibacterial halos were observed around the BMP-2(GelMA)@TiS and TiS scaffolds (Fig. 5G). Conversely, prominent zones of inhibition were observed around the RM-PLGA/BMP-2(GelMA)@TiS and RM-PLGA(GelMA)@TiS scaffolds. This was further confirmed through live/dead bacterial staining (Fig. 5H). In the RM-PLGA/BMP-2(GelMA)@TiS and RM-PLGA(GelMA)@TiS groups, large numbers of red-stained dead bacteria were observed, with only a few green-stained live bacteria. Conversely, the BMP-2(GelMA)@TiS and TiS groups displayed widespread green fluorescence, indicating a predominance of viable bacteria, with only sporadic red-stained dead cells. The relative quantification of live and dead bacteria is shown in Fig. 5I.

These findings demonstrate the robust *in vitro* antibacterial properties of the RM-PLGA/BMP-2(GelMA)@TiS composite scaffold.

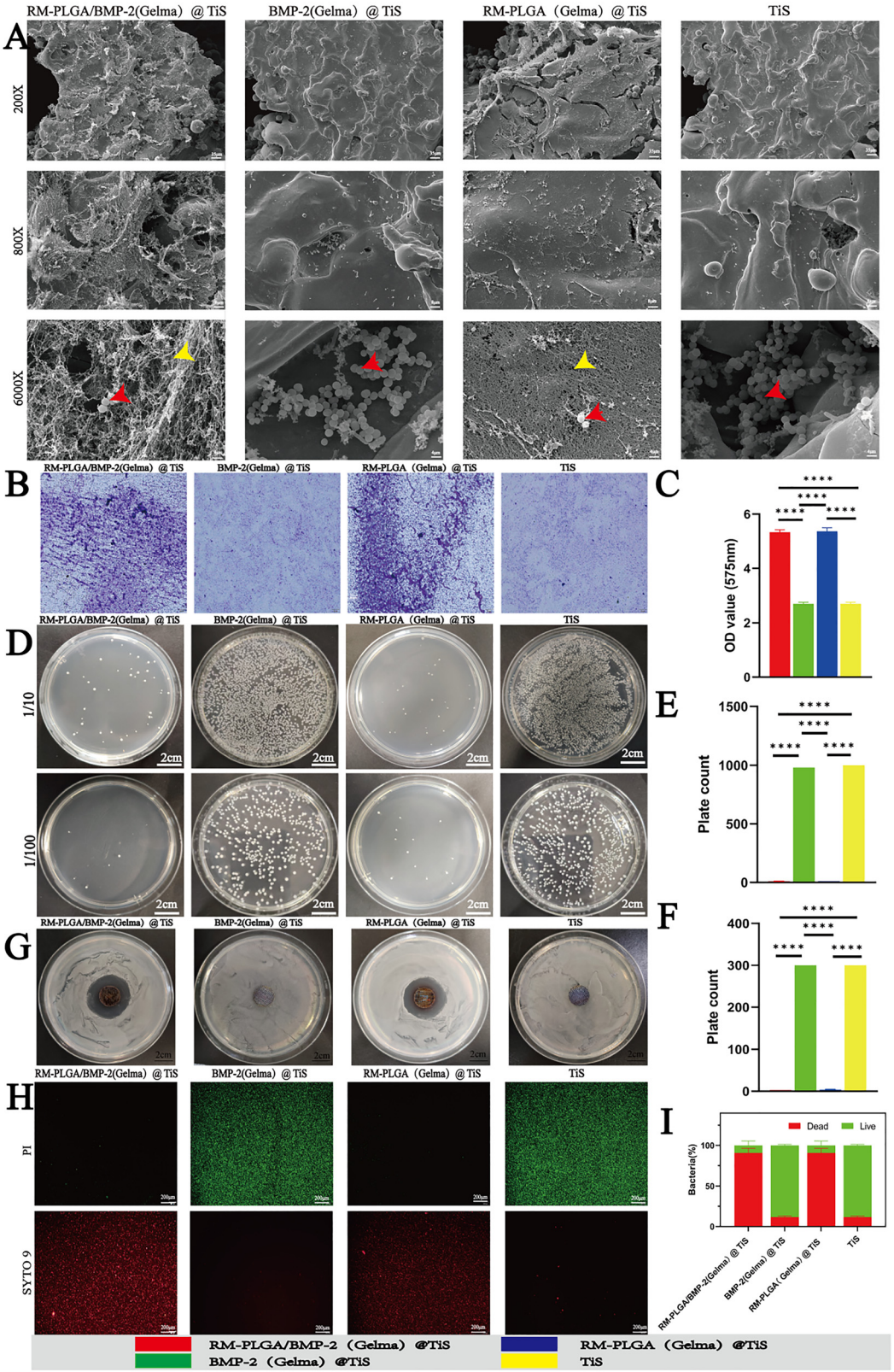

Fig. 5 (A) Scanning electron microscopy image of the composite scaffold co-cultured with bacteria. (B) Crystal violet staining of the bacterial biofilm. (C) Quantitative statistical graph of crystal violet staining. (D)–(F) Results and statistical graphs of plate toxicity tests with dilutions of 10 times and 100 times. (G) Antibacterial ring results. (H) Live/dead bacterial staining results. (I) Statistical graph of live/dead bacteria. $*p < 0.05$, $**p < 0.01$, $***p < 0.001$, $N = 3$.

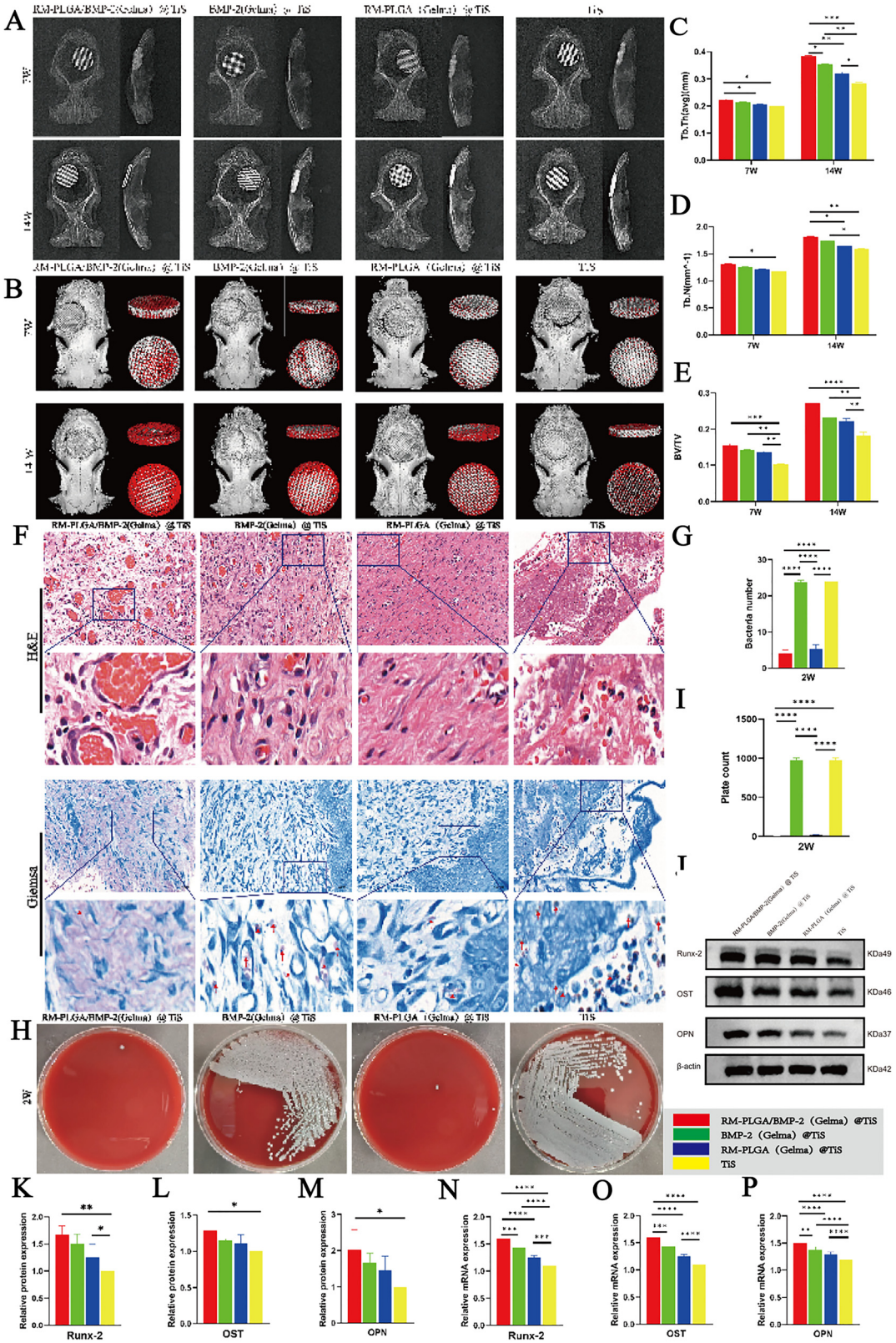

Fig. 6 (A) X-ray results at 7 weeks and 14 weeks after surgery. (B) Micro-CT results at 7 weeks and 14 weeks after surgery. (C)–(E) Three-dimensional reconstruction results of Tb.Th, Tb.N, and BV/TV. (F) and (G) HE staining, Giemsa staining, and bacterial quantity statistics at 2 weeks after surgery. (H) and (I) Soft tissue toxicity detection and statistical results at 2 weeks after surgery. (J)–(M) Western blot results and expression levels of Runx2, OST and OPN. (N)–(P) qPCR measurement results. *$p < 0.05$, **$p < 0.01$, ***$p < 0.001$, $N = 3$.

3.5. *In vivo* evaluation of RM-PLGA/BMP-2(GelMA)@TiS scaffolds

X-ray imaging at 7 and 14 weeks postoperatively revealed that the scaffolds in all groups remained securely in place, with no signs of loosening, dislodgement, surrounding bone fractures, or calvarial resorption (Fig. 6A). The results of micro-CT analysis and 3D reconstruction[32] are shown in Fig. 6B. By week 7, varying degrees of new bone formation were observed around and within the scaffold pores in all groups. However, translucent gaps remained visible between the scaffolds and the host calvarium. By week 14, the RM-PLGA/BMP-2(GelMA)@TiS group exhibited extensive new bone tissue surrounding the scaffold and filling its internal pores. The scaffold appeared well-integrated with the host bone, and its edges were tightly aligned with the margins of the defect, indicating a significant difference compared with the control groups, which showed less mature integration at the same time point. The quantitative analysis of trabecular bone parameters, including Tb.Th, Tb.N, and BV/TV (%), is shown in Fig. 6C–E. These parameters increased significantly over time across all groups. Notably, the RM-PLGA/BMP-2(GelMA)@TiS group exhibited significantly higher Tb.Th, Tb.N, and BV/TV values at both week 7 and week 14 compared with the control groups ($P < 0.05$).

At week 2, H&E staining and Giemsa staining, along with bacterial counting, in the control groups revealed significant neutrophil infiltration and dense bacterial colonization in the soft tissues surrounding the scaffolds, indicating a severe inflammatory response (Fig. 6F and G). In contrast, both the RM-PLGA-loaded groups exhibited markedly reduced numbers of infiltrating neutrophils and bacteria, accompanied by milder inflammatory reactions. Notably, the RM-PLGA/BMP-2(GelMA)@TiS group demonstrated clear signs of neovascularization. Blood agar plating and bacterial counting further confirmed that the number of bacteria in the control groups was significantly higher than that in the experimental groups (Fig. 6H and I). WB was performed to assess the expression of the osteogenic markers Runx2, osteocalcin, and osteopontin (Fig. 6J–M). The RM-PLGA/BMP-2(GelMA)@TiS group exhibited significantly elevated expression of all three markers compared with the control groups. These findings were corroborated by qPCR results (Fig. 6N–P). To further evaluate the potential biotoxicity of the implanted scaffolds, H&E staining was performed on the major organs (*i.e.*, heart, liver, spleen, lungs, and kidneys) of all rabbits.

In undecalcified hard tissue sections stained with H&E, the RM-PLGA/BMP-2(GelMA)@TiS group exhibited the highest levels of new bone formation and mineralization, in strong contrast to the control groups (Fig. 7A). Masson's trichrome staining yielded consistent results, with the RM-PLGA/BMP-2(GelMA)@TiS group showing the most prominent collagen deposition, neovascularization, and bone regeneration (Fig. 7B). In VG staining,[33] titanium appeared black, while newly formed bone was stained red (Fig. 7C). In the RM-PLGA/BMP-2(GelMA)@TiS group, a large amount of red-stained new bone had grown onto the scaffold struts, reaching maximum depth and coverage. The extent of new bone formation in this group was significantly greater than that in the control groups.

4. Discussion

The standard treatment for IBDs involves initial infection control followed by defect reconstruction. Persistent infection significantly hinders osteogenesis, as bacterial activity can further compromise local vascularization, expanding areas of bone necrosis. Therefore, the development of bifunctional bone scaffolds with both antibacterial and osteoinductive properties holds considerable promise for improving IBD outcomes. Compared to conventional 3D – printed bone scaffolds, triply periodic minimal surface (TPMS) structures exhibit unique biological advantages. The structural characteristics include: firstly, continuously smooth surfaces significantly reduce cellular shear stress. Secondly, highly interconnected porous networks effectively promote nutrient diffusion and directional cell migration. Thirdly, mechanical properties can be precisely regulated through mathematical parameters to achieve gradient matching with host bone tissue. Experimental data show that TPMS scaffolds achieve 10 times higher cell adhesion efficiency than traditional scaffolds, increase bone tissue regeneration rates by 30%, and demonstrate excellent resistance to cyclic loading, making them critically valuable for weight-bearing bone defect repair applications. A study by P. Vicky Kumar[23] introduced a PLA/$MgTiO_3$ composite scaffold that achieved over 90% inhibition of *Escherichia coli* through the release of antibacterial magnesium ions (Mg^{2+}). The scaffold's TPMS architecture, with over 70% porosity and interconnected channels, promoted physiological fluid circulation, reducing bacterial retention. Additionally, its surface roughness enhanced protein adsorption, synergistically improving both antibacterial efficacy and hydrophilicity, thereby accelerating bone ingrowth. In a previous study,[34] we incorporated antibiotic-loaded microspheres into 3D-printed scaffolds, demonstrating excellent anti-infective efficacy in both *in vitro* and *in vivo* IBDs models. However, most existing scaffold designs lack temporal coordination in functional delivery, failing to integrate the scaffold architecture, material composition, and drug release into a synergistic therapeutic system. More critically, they do not support a seamless transition from early-stage infection control to late-stage bone regeneration. To overcome these limitations, we employed 3D printing to fabricate a titanium scaffold with a gradient pore-sized TPMS structure, featuring 90% porosity at the periphery and 55% at the core. BMP-2 was incorporated into the smaller-pored inner region, whereas RM-PLGA microspheres were embedded in the larger-pored outer layer. The outer RM-PLGA microspheres facilitated sustained antibacterial activity in the early phase, creating a microenvironment conducive to osteogenesis. In the mid-to-late stages, BMP-2 released from the inner core promoted bone formation, while residual RM-PLGA microspheres maintained low-level antibacterial protection. This design establishes a spatiotemporally regulated release platform that dynamically modulates osteoblast and osteoclast activity for enhanced IBDs treatment.

SEM and EDS analyses confirmed the successful surface adherence and spatial distribution of RM-PLGA microspheres and BMP-2 on the titanium scaffold, with BMP-2 primarily

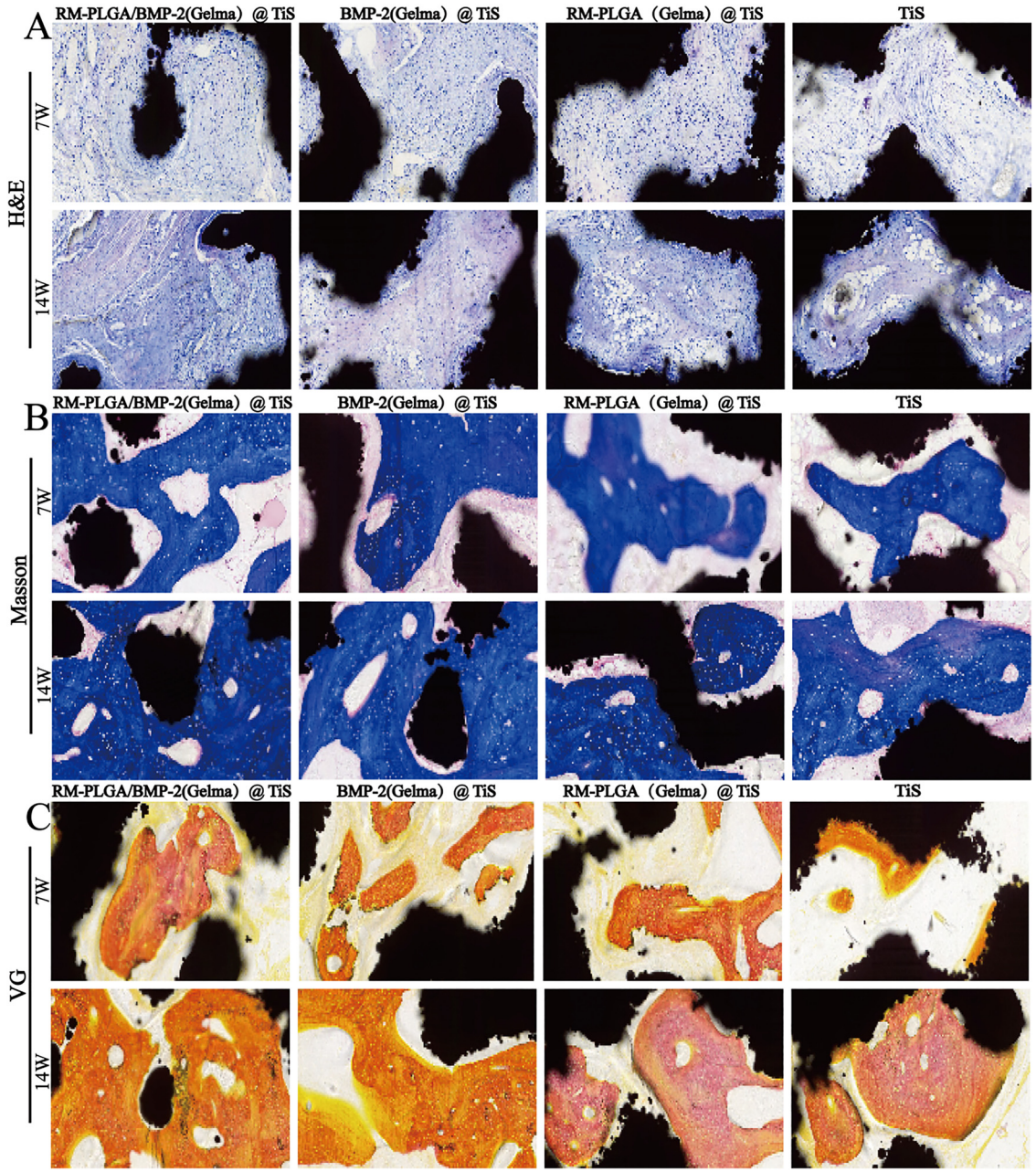

Fig. 7 (A) HE staining results of the stents in each group at 7 weeks and 14 weeks after surgery. (B) Masson staining results of the stents in each group at 7 weeks and 14 weeks after surgery. (C) VG staining results of the stents in each group at 7 weeks and 14 weeks after surgery. *$p < 0.05$, **$p < 0.01$, ***$p < 0.001$, $N = 3$.

localized in the inner porous regions and RM-PLGA microspheres in the outer layer. Drug release profiles validated this design: Mox and Rif exhibited rapid initial release followed by sustained release through the mid-to-late stages, while BMP-2 release became prominent around day 10. This spatiotemporal release supports the scaffold's intended functionality, *i.e.*, early antibacterial activity transitioning to osteoinductive stimulation. Such a strategy effectively meets the therapeutic needs of IBDs across distinct healing phases, offering a novel approach for dynamic, staged bone repair. *In vitro*, both BMP-2-loaded groups showed enhanced cellular adhesion and proliferation, confirming BMP-2's excellent biocompatibility. Osteogenic differentiation assays, including collagen fiber staining, ALP staining and quantification, and alizarin red S staining, demonstrated significantly superior outcomes in BMP-2-loaded groups compared with control groups. These findings indicate that BMP-2 promotes the directed differentiation and proliferation of mesenchymal stem cells into chondrocytes and osteoblasts, enhances osteoblast maturation, and plays a key role in bone and cartilage development and remodeling, thereby accelerating bone defect repair. Antibacterial assessments revealed that RM-PLGA-loaded groups exhibited significantly larger

inhibition zones, greater biofilm necrosis, and a higher proportion of dead bacteria than control groups, confirming the potent and sustained antibacterial activity of RM-PLGA microspheres. X-ray imaging and micro-CT 3D reconstruction distinguished mature and newly formed bone. The RM-PLGA/BMP-2(GelMA)@TiS scaffold demonstrated tight integration with host bone at the defect margins and was extensively surrounded and infiltrated by new bone tissue, both peripherally and within the scaffold pores. In contrast, control groups showed persistent voids and significantly lower trabecular parameters (Tb.Th, Tb.N, and BV/TV). H&E and Giemsa staining at week 2 revealed minimal neutrophil infiltration and bacterial presence in the RM-PLGA/BMP-2(GelMA)@TiS group, indicating a mild inflammatory response. Neovascularization was also notably increased. Blood agar plating showed an absence of SA colonies, confirming the scaffold's sustained and targeted antibacterial effect. This dual-antibiotic system leverages agents capable of penetrating the "blood–bone barrier." Mox, a fourth-generation fluoroquinolone, offers high intraosseous bioavailability and strong cellular penetration, enabling the eradication of intracellular SA. Rif, used in combination therapy, reduces resistance development and significantly improves osteomyelitis outcomes. These characteristics explain the superior bactericidal efficacy of RM-PLGA-loaded scaffolds. Runx2 is a transcription factor essential for osteoblast differentiation, OPN promotes mineralization and bone remodeling, and OST is a major non-collagenous bone matrix protein involved in calcium homeostasis. The WB target protein has polyclonal antibodies.[35]The upregulation of these osteogenic markers suggests that the RM-PLGA/BMP-2(GelMA)@TiS scaffold promotes new bone formation by modulating the expression of Runx2, OPN, and OST, as further supported by qPCR results. Histological assessments using H&E and Masson's trichrome staining showed that the RM-PLGA/BMP-2(GelMA)@TiS group exhibited the highest levels of new bone formation and mineralization, along with pronounced collagen deposition, angiogenesis, and overall bone regeneration. H&E staining provided detailed morphological insights into the regenerated tissue architecture, while Masson's staining revealed the organization and distribution of fibrous tissue. Together, these findings indicate that the scaffold markedly enhanced bone repair. Additionally, VG staining confirmed strong integration between the newly formed bone and the scaffold, with bone tissue firmly adhering to the strut surfaces. Extensive red-stained bone infiltrating deep into the scaffold, along with substantial deposition of cellular surface markers and collagen, further validated the scaffold's excellent osteoregenerative potential.

These favorable outcomes are largely attributable to the optimized design of the TPMS titanium scaffold, which features a peripheral porosity of 90% and a central porosity of 55%. This configuration provided sufficient internal volume for effective DL while maintaining mechanical stability. The carefully selected pore size (420–630 μm) enhanced waste clearance, nutrient diffusion, and surface area for bone ingrowth while supporting localized and controlled release of bioactive agents. By integrating material innovation, structural optimization, and functional modularity, the 3D-printed scaffold established a dynamic therapeutic platform characterized by early-stage antibacterial activity followed by mid-to-late-stage osteoinductive stimulation.

One limitation of this study is the lack of a comparative analysis evaluating how different porosity ratios affect the loading efficiency of RM-PLGA and BMP-2, particularly in relation to antibacterial activity and bone regeneration. Additionally, the relatively small sample size may limit the generalizability of the findings. Future studies should include larger and more diverse cohorts to validate these results.

5. Conclusions

Herein, we successfully fabricated a 3D-printed titanium scaffold featuring a gradient porosity ranging from 55% at the center to 90% at the periphery, with pore sizes between 420 and 630 μm. The scaffold was engineered for spatially selective loading: RM-PLGA microspheres were incorporated into the outer pores and BMP-2 into the inner pores, with the GelMA hydrogel serving as a coating matrix to enable dual-stage drug delivery. This design facilitates sustained antibacterial activity during the early phase *via* RM-PLGA microspheres, followed by predominant BMP-2 release during the mid-to-late phase, while residual microspheres continue to provide antibacterial protection. The spatiotemporally regulated release system effectively modulates osteoblast and osteoclast activity. *In vitro* assays demonstrated that the RM-PLGA/BMP-2(GelMA)@TiS scaffold exhibits excellent sustained antibacterial activity, cytocompatibility, osteogenic differentiation capacity, and extracellular matrix mineralization. *In vivo* studies further confirmed that the scaffold can suppress SA-induced osteomyelitis while promoting robust bone regeneration. These findings present a promising therapeutic strategy and biomaterial platform for the treatment of infectious bone defects.

Ethics statement

The animal experiments in this study were carried out in compliance with the relevant national and institutional guidelines for the care and use of laboratory animals. The experimental protocol was approved by the Laboratory Animal Center of Ningxia Medical University, with the approval number IACUC-H2025003.

Conflicts of interest

The author declares that there are no conflicts of interest.

Data availability

I agree to provide the data and materials that support the results or analyses in the paper. My information will be made available upon reasonable request.

Supplementary information (SI) is available. See DOI: **https://doi.org/10.1039/d5tb02071a**.

Acknowledgements

This research was supported by the National Natural Science Foundation of China (grant no. 82460431) and the Ningxia Natural Science Foundation (grant no. 2023AACO2064).

References

1 S. Zhang, Z. Lian and X. Chen, *et al.*, Preparation and properties of chitosan quaternary ammonium salt/α-calcium sulfate hemihydrate/β-tricalcium phosphate composite bone cement, *Colloids Surf., B*, 2025, **253**, 114738, DOI: **10.1016/j.colsurfb.2025.114738**.

2 E. Woussen, Z. Aouzal and I. Pluvy, *et al.*, Hand and wrist Osteo-articular bone defect: induced membrane technique indications, *Hand Surg. Rehabilitat.*, 2023, **42**(2), 160–167, DOI: **10.1016/j.hansur.2023.01.005**.

3 J. E. Hellwinkel, Z. M. Working and L. Certain, *et al.*, The intersection of fracture healing and infection: Orthopaedics research society workshop 2021, *J. Orthop. Res.*, 2022, **40**(3), 541–552, DOI: **10.1002/jor.25261**.

4 K. Li, S. Yu and D. Lin, *et al.*, Imaging observation of allogeneic bone and bone-induced calcium phosphate biomaterials as supplements in the treatment of infectious bone defects, *J. Orthop. Surg.*, 2025, **33**(2), 10225536251362765, DOI: **10.1177/10225536251362765**.

5 H. Zhang, W. Qiao and Y. Liu, *et al.*, Addressing the challenges of infectious bone defects: a review of recent advances in bifunctional biomaterials, *J. Nanobiotechnol.*, 2025, **23**(1), 257, DOI: **10.1186/s12951-025-03295-0**.

6 N. Abedi, A. Sadeghian and M. Kouhi, *et al.*, Immunomodulation in Bone Tissue Engineering: Recent Advancements in Scaffold Design and Biological Modifications for Enhanced Regeneration, *ACS Biomater. Sci. Eng.*, 2025, **11**(3), 1269–1290, DOI: **10.1021/acsbiomaterials.4c01613**.

7 Z. Chen, Y. Yang and B. Liu, *et al.*, Application of 3D-printed porous prosthesis for the reconstruction of infectious bone defect with concomitant severe soft tissue lesion: a case series of 13 cases, *BMC Musculoskeletal Disord.*, 2024, **25**(1), 1090, DOI: **10.1186/s12891-024-08248-6**.

8 L. Pitol-Palin, J. Moura and P. B. Frigério, *et al.*, A preliminary study of cell-based bone tissue engineering into 3D-printed β-tricalcium phosphate scaffolds and polydioxanone membranes, *Sci. Rep.*, 2024, **14**(1), 31184, DOI: **10.1038/s41598-024-82334-6**.

9 W. L. Ng, J. An and C. K. Chua, Process, Material, and Regulatory Considerations for 3D Printed Medical Devices and Tissue Constructs, *Engineering*, 2024, **36**, 146–166, DOI: **10.1016/j.eng.2024.01.028**.

10 A. Farazin and S. Mahjoubi, Dual-functional Hydroxyapatite scaffolds for bone regeneration and precision drug delivery, *J. Mech. Behav. Biomed. Mater.*, 2024, **157**, 106661, DOI: **10.1016/j.jmbbm.2024.106661**.

11 Y. Zhang, M. Zhang and M. Li, *et al.*, Icariin-Enhanced Osteoclast-Derived Exosomes Promote Repair of Infected Bone Defects by Regulating Osteoclast and Osteoblast Communication, *Int. J. Nanomed.*, 2024, **19**, 12389–12407, DOI: **10.2147/ijn.S483621**.

12 S. Kanwar and S. Vijayavenkataraman, Design of 3D printed scaffolds for bone tissue engineering: A review, *Bioprinting*, 2021, **24**, e00167, DOI: **10.1016/j.bprint.2021.e00167**.

13 X. Hu, J. Chen and S. Yang, *et al.*, 3D Printed Multifunctional Biomimetic Bone Scaffold Combined with TP-Mg Nanoparticles for the Infectious Bone Defects Repair, *Small*, 2024, **20**(40), e2403681, DOI: **10.1002/smll.202403681**.

14 Z. Han, J. Xiong and X. Jin, *et al.*, Advances in reparative materials for infectious bone defects and their applications in maxillofacial regions, *J. Mater. Chem. B*, 2024, **12**(4), 842–871, DOI: **10.1039/d3tb02069j**.

15 Y. Sun, Y. Zhang and K. Zhang, *et al.*, Mechanochemically reprogrammed porous tantalum with synergistic antibacterial and osteogenic properties for the treatment of infectious bone defects, *J. Nanobiotechnol.*, 2025, **23**(1), 552, DOI: **10.1186/s12951-025-03610-9**.

16 J. Jin, X. Xia and C. Ruan, *et al.*, GAPDH-Silence Microsphere via Reprogramming Macrophage Metabolism and eradicating Bacteria for Diabetic infection bone regeneration, *J. Nanobiotechnol.*, 2024, **22**(1), 517, DOI: **10.1186/s12951-024-02787-9**.

17 W. Xiong, L. Yuan and L. Wang, *et al.*, [Preparation of berberine-naringin dual drug-loaded composite microspheres and evaluation of their antibacterial-osteogenic properties], Zhongguo xiu fu chong jian wai ke za zhi = Zhongguo xiufu chongjian waike zazhi, *Chin. J. Repar. Reconstr. Surg.*, 2023, **37**(12), 1505–1513, DOI: **10.7507/1002-1892.202308054**.

18 J. Li, K. Li and Y. Du, *et al.*, Dual-Nozzle 3D Printed Nano-Hydroxyapatite Scaffold Loaded with Vancomycin Sustained-Release Microspheres for Enhancing Bone Regeneration, *Int. J. Nanomed.*, 2023, **18**, 307–322, DOI: **10.2147/ijn.S394366**.

19 K. Elkhoury, D. Patel and N. Gupta, *et al.*, Nanocomposite GelMA Bioinks: Toward Next-Generation Multifunctional 3D-Bioprinted Platforms, *Small*, 2025, e05968, DOI: **10.1002/smll.202505968**.

20 J. Ye, Y. Li and X. Yin, Salvianolic acid B ameliorates vascular calcification in rats with chronic kidney disease combined with arteriovenous fistula by inhibiting BMP2/Smads signaling, *Renal Failure*, 2025, **47**(1), 2542524, DOI: **10.1080/0886022x.2025.2542524**.

21 M. Salehi Namini, S. Mohandesnezhad and S. Mohandesnezhad, *et al.*, Enhancing bone regeneration using kaempferol as an osteoprotective compound: signaling mechanisms, delivery strategies, and potential applications, *J. Biol. Eng.*, 2025, **19**(1), 74, DOI: **10.1186/s13036-025-00545-5**.

22 F. Xiao, G. H. Ren and C. Y. Pan, *et al.*, Design and in vitro evaluation of gradient Schwarz Primitive scaffolds with thin-board integration for bone implants, *Biomater. Adv.*, 2025, **177**, 214412, DOI: **10.1016/j.bioadv.2025.214412**.

23 P. V. Kumar, S. Pal and A. K. Birru, *et al.*, 3D-printed TPMS-structured hybrid PLA/MgTiO(3) scaffolds: Synergizing bioactivity and antibacterial performance for bone regeneration, *Biomater. Adv.*, 2025, **177**, 214370, DOI: **10.1016/j.bioadv.2025.214370**.

24 H. Kim, S. Kim and H. S. Han, *et al.*, Improved bone regeneration with bone targeted scaffold, *Sci. Rep.*, 2025, **15**(1), 27002, DOI: **10.1038/s41598-025-12497-3**.

25 M. Jafarbeglou, A. Meimandi-Parizi and A. Derakhshandeh, *et al.*, Silk fibroin/chitosan thiourea hydrogel scaffold with vancomycin and quercetin-loaded PLGA nanoparticles for treating chronic MRSA osteomyelitis in rats, *Int. J. Pharm.*, 2024, **666**, 124826, DOI: 10.1016/j.ijpharm.2024.124826.

26 J. M. Saul, J. S. Bohnert and M. O'Brien, *et al.*, Keratin Scaffold Formulation Impacts rhBMP-2 Biodistribution and Bone Regeneration in a Rat Femur Defect Model, *Tissue Eng. Regener. Med.*, 2025, DOI: 10.1007/s13770-025-00747-4.

27 E. Eren Belgin and C. G. Delibalta, Quaternized chitosan/PVA/natural bioactive agent electrospun wound scaffolds: production, characterization, and investigation of release kinetics, *Turk. J. Chem.*, 2023, **47**(6), 1529–1539, DOI: 10.55730/1300-0527.3633.

28 D. Abdelmoneim, D. Coates and G. Porter, *et al.*, In vitro and in vivo investigation of antibacterial silver nanoparticles functionalized bone grafting substitutes, *J. Biomed. Mater. Res. Part A*, 2024, **112**(12), 2042–2054, DOI: 10.1002/jbm.a.37757.

29 J. A. Rincón-López, J. A. Hermann-Muñoz and R. Detsch, *et al.*, Mineral matrix deposition of MC3T3-E1 pre-osteoblastic cells exposed to silicocarnotite and nagelschmidtite bioceramics: In vitro comparison to hydroxyapatite, *J. Biomed. Mater. Res. Part A*, 2024, **112**(7), 1124–1137, DOI: 10.1002/jbm.a.37699.

30 M. H. Chien, C. Y. Chen and C. L. Yeh, *et al.*, Biofabricated poly (γ-glutamic acid) bio-ink reinforced with calcium silicate exhibiting superior mechanical properties and biocompatibility for bone regeneration, *J. Dental Sci.*, 2024, **19**(1), 479–491, DOI: 10.1016/j.jds.2023.09.008.

31 S. Chen, R. Guo and Q. Liang, *et al.*, Multifunctional modified polylactic acid nanofibrous scaffold incorporating sodium alginate microspheres decorated with strontium and black phosphorus for bone tissue engineering, *J. Biomater. Sci. Polym. Ed.*, 2021, **32**(12), 1598–1617, DOI: 10.1080/09205063.2021.1927497.

32 X. Wu, Z. Q. Wang and J. J. Wei, *et al.*, [Effects of isopsoralen on tibial fracture and vascular healing in mice], Zhongguo gu shang =, *Chin. J. Orthop. Traumatol.*, 2023, **36**(12), 1169–1176, DOI: 10.12200/j.issn.1003-0034.2023.12.012.

33 Z. Liu, Z. Xu and X. Wang, *et al.*, Construction and osteogenic effects of 3D-printed porous titanium alloy loaded with VEGF/BMP-2 shell-core microspheres in a sustained-release system, *Front. Bioeng. Biotechnol.*, 2022, **10**, 1028278, DOI: 10.3389/fbioe.2022.1028278.

34 Z. Qiao, W. Zhang and H. Jiang, *et al.*, 3D-printed composite scaffold with anti-infection and osteogenesis potential against infected bone defects, *RSC Adv.*, 2022, **12**(18), 11008–11020, DOI: 10.1039/d2ra00214k.

35 S. Shahmohammadi-Farid, R. Ghods and M. Jeddi-Tehrani, *et al.*, Generation and Characterization of Siglec-F-Specific Monoclonal Antibodies, *Iran. J. Allergy, Asthma Immunol.*, 2017, **16**(6), 460–470.

